

Constraints on the Spin-Pole Orientation, Jet Morphology and Rotation of Interstellar Comet 2I/Borisov with Deep *HST* Imaging

Bryce T. Bolin^{1,2*} and Carey M. Lisse³

¹*Division of Physics, Mathematics and Astronomy, California Institute of Technology, Pasadena, CA 91125, U.S.A.*

²*IPAC, Mail Code 100-22, Caltech, 1200 E. California Blvd., Pasadena, CA 91125, U.S.A.*

³*Johns Hopkins University Applied Physics Laboratory, Laurel, MD 20723, U.S.A.*

Accepted 23 July 2020. Received 3 June 2020; in original form 5 May 2020

ABSTRACT

We present high resolution, deep imaging of interstellar comet 2I/Borisov taken with the *Hubble Space Telescope*/Wide Field Camera 3 (*HST*/WFC3) on 2019 December 8 UTC and 2020 January 27 UTC (HST GO 16040, PI Bolin) before and after its perihelion passage in combination with *HST*/WFC3 images taken on 2019 October 12 UTC and 2019 November 16 UTC (HST GO/DD 16009, PI Jewitt) before its outburst and fragmentation of March 2020, thus observing the comet in a relatively undisrupted state. We locate 1-2'' long (2,000 - 3,000 km projected length) jet-like structures near the optocenter of 2I that appear to change position angles from epoch to epoch. With the assumption that the jet is located near the rotational pole supported by its stationary appearance on ~10-100 h time frames in *HST* images, we determine that 2I's pole points near $\alpha = 322 \pm 10^\circ$, $\delta = 37 \pm 10^\circ$ ($\lambda = 341^\circ$, $\beta = 48^\circ$) and may be in a simple rotation state. Additionally, we find evidence for possible periodicity in the *HST* time-series lightcurve on the time scale of ~5.3 h with a small amplitude of ~0.05 mag implying a lower limit on its b/a ratio of ~1.5 unlike the large ~2 mag lightcurve observed for 1I/'Oumuamua. However, these small lightcurve variations may not be the result of the rotation of 2I's nucleus due to its dust-dominated light-scattering cross-section. Therefore, uniquely constraining the pre-Solar System encounter, pre-outburst rotation state of 2I may not be possible even with the resolution and sensitivity provided by *HST* observations.

Key words: Minor planets – Comets – galaxy: local interstellar matter

1 INTRODUCTION

The second interstellar object, 2I/Borisov (hereafter 2I), has had a morphological appearance similar to Solar System comets ever since its discovery (Guzik et al. 2019; Bolin et al. 2020a). Cometary gas measurements have revealed CO (Bodewits et al. 2020; Cordiner et al. 2020), and [O I] resulting from photodissociation of H₂O (McKay et al. 2019; Crovisier et al. 2019), and the typical visible-wavelength daughter species (e.g., CN and C₂ Fitzsimmons et al. 2019; Opitom et al. 2019; Bannister et al. 2020). The comet seems to have a high CO abundance but may be carbon-chain depleted (A'Hearn et al. 1995; Kareta et al. 2019).

The color and activity of 2I have been revealed to be similar to that of Solar System comets. Visible to near-infrared photometry and spectra of the comet are reddish to neutral suggesting the presence of refractory organics and water-ice common in comets (de León et al. 2019; Bolin et al. 2020a; Yang et al. 2020). Additionally, its activity has been revealed by long-term lightcurve trending to be driven by super-volatiles such as CO/CO₂ far from the Sun, with the addition of H₂O-driven activity as the comet crossed inside 3-4 au on its way to a ~2 au perihelion distance (Bolin et al. 2020a; Ye et al. 2019; Cremonese et al. 2020). Constraints on 2I's size from gas production rates (Fitzsimmons et al. 2019), statistical

* E-mail: bbolin@caltech.edu (BTB)

Table 1. WFC3/UVIS F350LP equivalent V-band photometry and viewing geometry.

Date ¹ (UTC)	H^2	σ_H^3	r_h^4 (au)	Δ^5 (au)	α^6 ($^\circ$)	δ_\oplus^7 ($^\circ$)	b^8 ($^\circ$)	PA ⁹ ($^\circ$)	PID ¹⁰
2019 Oct 12	16.59	0.03	2.38	2.79	20.26	-14.23	46.77	180	GO/DD 16009
2019 Nov 16	16.57	0.03	2.07	2.21	26.49	-17.55	48.87	210	GO/DD 16009
2019 Dec 8	16.54	0.04	2.01	1.99	28.49	-15.88	40.58	235	GO 16040
2020 Jan 27	16.59	0.04	2.29	2.04	25.51	-0.66	10.30	250	GO 16040

- (1) Date of observation, (2) H magnitude using a 0.2'' radius aperture and 0.2-0.8'' sky and outer coma subtraction annulus and Eq. 1, (3) V magnitude uncertainty, (4) heliocentric distance, (5) geocentric distance, (6) phase angle, (7) Earth and target orbital plane angle, (8) galactic latitude of observations, (9) position angle of jet, (10) *HST* program ID.

arguments (Jewitt & Luu 2019), high resolution adaptive optics imaging from ground-based facilities (Bolin et al. 2020a) suggest a nucleus \sim km-scale diameter. However, direct detection of the nucleus has not yet been possible due to the total brightness of the coma obscuring the nucleus (Jewitt & Luu 2019).

In this paper, we present high resolution and deep stack optical observations made with the *Hubble Space Telescope* to study the coma structure of 2I. In particular, our observations are relevant in studying the comet before it underwent a 0.7 magnitude outburst on 2020 March 7 UTC, 2I (Drahus et al. 2020; Jehin et al. 2020). Subsequent HST observations in late 2020 March revealed that 2I was undergoing fragmentation in possible connection to the outburst (Bolin et al. 2020b; Jewitt et al. 2020b). Regardless of the cause of its outburst, we present these observations as indicative of 2I in its pre-outburst state before fragmentation may have had an affect on its physical properties and rotation.

2 OBSERVATIONS

The *Hubble Space Telescope* (*HST*) was used to observe 2I with General Observer's (GO) time on 2019 December 8 UTC and 2020 January 27 UTC (HST GO 16040, PI Bolin et al. 2019). Two orbits were used to observe 2I on 2019 December 8 UTC and two more orbits were used on 2020 January 27 UTC. During each orbit on 2019 December 8 UTC, one 404 s F689M filter exposure and one 404 s F845M filter exposure was obtained with the UVIS2 array of the WFC3/UVIS camera (Dressel 2012) for a total of 4 exposures and 1616 s integration time over both orbits. For the two orbit observations of 2I on 2020 January 27 UTC, two 386 s exposures were obtained in the F689M and in the F845M filter for a total exposure time of 1544 s. The F689M filter has a central wavelength of 688.32 nm with a FWHM bandpass of 70.76 nm and the F845M filter has a central wavelength of 846.40 nm with a FWHM bandpass of 88.07 nm (Deustua et al. 2017). The comet was observed on two back-to-back orbits and was tracked non-sidereally.

As already described in (Manzini et al. 2020; Kim et al. 2020), *HST* was used to observe 2I with director's discretionary time on 2019 October 12 UTC (HST GO/DD 16009, Jewitt et al. 2020a). Up to seven orbits were awarded for the director's discretionary time, with four orbits were used on 2019 October 12 UTC to observe 2I. During each orbit on 2019 October 12 UTC, six 260 s F350LP filter exposures were obtained with the 2K subarray of the WFC3/UVIS camera for a total of 24 exposures and 6240 s integration time. The F350LP filter has a central wavelength of 581.95 nm with a FWHM bandpass of 489.26 nm (Deustua et al. 2017). The comet was observed on four back-to-back orbits and was tracked non-sidereally at its rate of sky motion. Additional observations of 2I were conducted with one orbit of *HST* on 2019 November 16 UTC. Six 230 s exposures were taken with the F350LP filter tracking on its rate of motion, though only four of the 230 s exposures were used from November 16 UTC because the coma of 2I significantly overlapped with an extended background galaxy in two of the 230 s exposures resulting in a total exposure time of 920 s. The viewing geometry of 2I during all of the *HST* observations described here are available in Table 1. The resolution element in all imaging data presented here is 0.04''/pixel.

3 RESULTS

3.1 Morphology and Jets

The two 404 s F689M filter exposures and two 404 s F845M filter obtained on 2019 December 8 UTC under HST GO 16040 were aligned and median stacked into a single composite image with an equivalent exposure time of 1616 s. Cosmic ray removal was done within the vicinity of the comet by interpolating any regions of the chip affected by cosmic rays with the average pixel values of regions surrounding the cosmic ray strikes. The composite stacks were enhanced by normalizing the radial profile of the coma originating from the optocenter in the images. The enhanced coma removed images from 2019 December 8 UTC are presented in the third column of Fig. 1. The fourth column of Fig. 1 presents a composite 1544 s stack of two F689M filter images and two F845M images. The streaked background in the 2020 January 27 UTC composite images is due to imperfect removal of dense background star fields at the 10.3 $^\circ$ galactic latitude the images were taken. We combine our

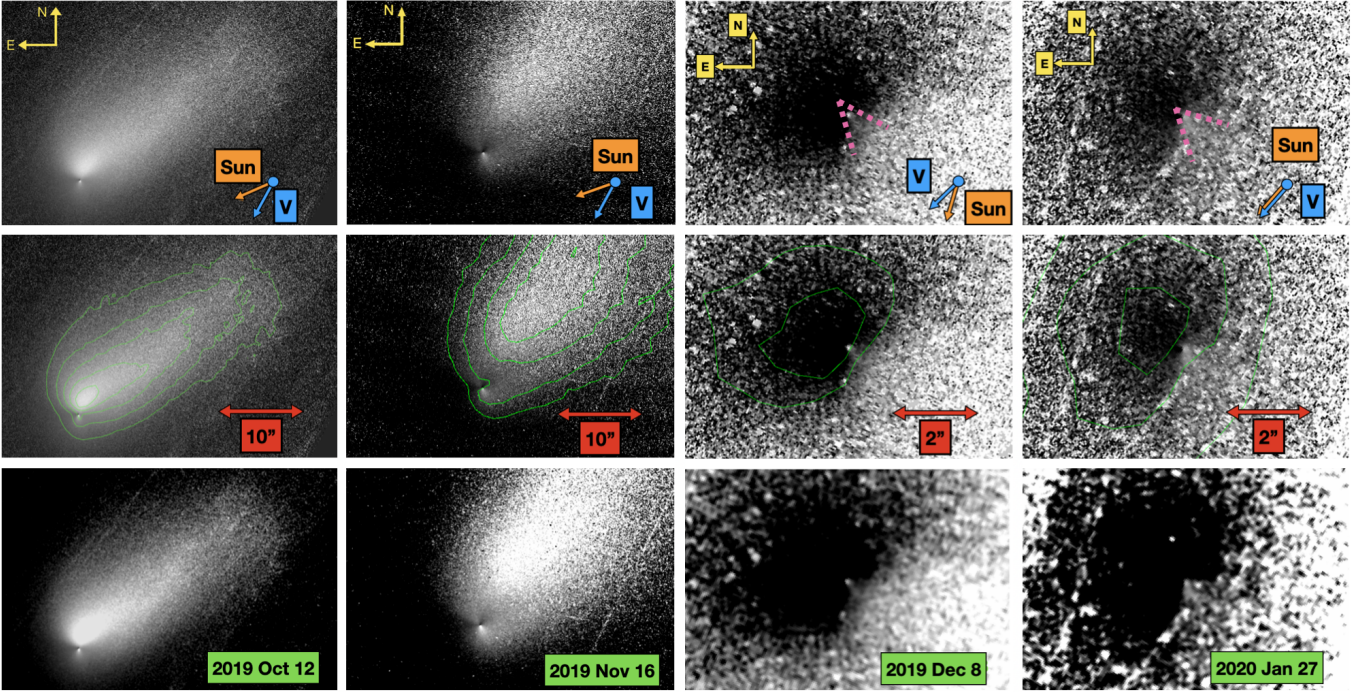


Figure 1. Mosaic of composite images of 2I taken with *HST* on 2019 October 12 UTC and 2019 November 16 UTC using the F350LP filter (HST GO/DD 16009, Jewitt et al. 2019a; Kim et al. 2020) and on 2019 December 8 UTC and 2020 January 27 UTC using the F689M and F845M filters (HST GO 16040, Bolin et al. 2019). Left column, top panel: 2019 October 12 UTC median stack of 24 x 260 s F350LP exposures taken on subsequent orbits with the radial profile of the coma removed. The pixel scale is $0.04''/\text{pixel}$. Left column, center panel: contour plot of the surface brightness profile of 2I over-plotted on the composite WFC3/UVIS image. $10''$ is equivalent to $\sim 20,000$ km at the geocentric distance of the comet of 2.79 au on 2019 October 12 UTC. Left column, bottom panel: Gaussian-smoothed version of the coma profile removed *HST* composite image. Second left column: the same as the left panel, 2019 November 16 UTC median stack of 4 x 230 s F350LP exposures with the radial profile of the coma removed. $10''$ is equivalent to $\sim 16,000$ km at the geocentric distance of the comet of 2.21 au on 2019 November 16 UTC. Third column: 2019 December 8 UTC median stack of 2 x 404 s F689M and 2 x 404 s F845M exposures with the radial profile of the coma removed. $2''$ is equivalent to $\sim 2,900$ km at the geocentric distance of the comet of 1.99 au on 2019 December 8 UTC. The pink dotted wedges in the top panel highlights the location of the jet. Fourth column: 2020 January 27 UTC median stack of 2 x 386 s F689M and 2 x 386 s F845M exposures with the radial profile of the coma removed. $2''$ is equivalent to $\sim 3,000$ km at the geocentric distance of the comet of 2.04 au on 2020 January 27 UTC. The artifacts on the west side of the image is from incomplete removal of background stars at the low $\sim 10.3^\circ$ galactic latitude of the observations.

HST GO 16040 images with images taken by HST GO/DD 16009 (PI Jewitt et al. 2019a) on 2019 October 12 UTC and 2019 November 16 UTC. The 24 F350LP images obtained were median binned and cosmic ray removed identically to the F689M and F845M images. The enhanced F350LP coma removed images are also presented in the left-most column on Fig. 1.

In the *HST* observations on 2019 October 12 UTC, a clear tail is present in excess of $30''$, as also seen in the ground-based observations (Jewitt & Luu 2019; Bolin et al. 2020a), with a position angle opposite of the orbital velocity indicating the presence of 100 micron-sized dust grains (Jewitt et al. 2020a; Kim et al. 2020). However, the position angle of the tail may also be compatible with grains moving in the anti-solar direction; the two cases are difficult to distinguish due to projection effects at the modest orbital plane angle between *HST* and the comet at the time of the observations. The enhanced coma removed images for the 2019 November 16 data are presented in the column second from the left on Fig. 1. The comet had a heliocentric distance of 2.07 au, a geocentric distance of 2.21 au, a phase angle of 26.49° and an orbital plane angle of -17.55° on 2019 November 16 UTC.

For the data taken on 2020 October 12 UTC presented in the center-left panel of Fig. 1, contours showing the structure of the tail and jet are over-plotted on the radial profile normalized composite image show an enhancement in surface brightness of the coma near its center. A smoothed-version of the radial profile normalized image is shown in the bottom left panel revealing an azimuthally asymmetric surface brightness profile within $5''$ of the center of the coma at position angles 0° and 180° (Jewitt et al. 2020a; Manzini et al. 2020; Kim et al. 2020). The thin southern surface brightness enhancement at a position angle of $\sim 180^\circ$, more easily seen in the left panel's bottom image of Fig. 1 that has been smoothed with a Gaussian filter to enhance low surface brightness features, may be interpreted as a localized jet, as seen in some Solar System comets (e.g., Farnham 2009; Knight & Schleicher 2013; Bodewits et al. 2018). The position angle of the jet has been estimated by the location of the peak brightness in the jet's radial profile drawn from the center of the nucleus in azimuthal coordinates

with an origin of 0° pointing north (e.g., [Farnham & Cochran 2002](#)). There was no indication that the position angle of the jet showed significant variation or curvature as a function of radial distance from the coma even after the application of radial coma removal and smoothing contrast enhancement techniques ([Schleicher & Farnham 2004](#)).

The F350LP data from 2019 November 16 UTC were also median stacked with a total equivalent exposure time of 920 s with the coma's radial profile normalized as seen in the second left column of Fig. 1. Similarly, both jets are seen in the 2019 October 12 data appear in the 2019 November 16 UTC data in the third column of Fig. 1 with position angles of $\sim 30^\circ$ and $\sim 210^\circ$ as seen in the second column of Fig. 1. The south-pointing jet is seen again in the 2019 December 8 UTC F689M + F845M data with a position angle of $\sim 235^\circ$ as seen in the third column of Fig. 1. The north-facing jet is not visible in the 2019 December 8 UTC data, however, it is visible in F350LP data taken on 2020 December 9 UTC and has an angle of $\sim 60^\circ$ possible due to the greater sensitivity of the 2020 December 9 F350LP observations (see Fig. 6 [Manzini et al. 2020](#)).

A 1544 s F689M + F845M composite stack taken on 2020 January 27 UTC when the comet was passing through the orbital plane is shown in the right column of Fig. 1 indicating that the tail of 2I has a wide fan-like projection in excess of $\sim 4''$ and the presence of a jet with a position angle of $\sim 250^\circ$ and $\sim 20^\circ$ wide while tail at an Earth and target orbital plane angle of $< 1^\circ$. However, measuring the perpendicular velocity dispersion of dust consisting of the width of the tail is beyond the scope of this work due to the uncertainty in the timing of the ejection of the material. Observing the comet at this small orbital plane angle reveals the perpendicular to orbital vector extent of the tail perpendicular to the comet's orbital plane with minimum projection effects. The north-facing, 0° feature seen on 2019 October 12 has completely disappeared in the 2020 January 27 UTC image suggesting that projection or varying illumination effects may be concealing it or changing the level of activity during the 2020 January 27 UTC observations. The possibility of varying solar illumination on various latitudes of the comet's surface on the apparent disappearance of the northward jet is also discussed below. We do not think that the small long-term change in jet position angle between 2019 October 12 UTC and 2019 December 23 UTC is indicative of a new region becoming active, but we assume is instead due to the small changes in viewing geometry between these observations as explained in Section 3.2.

3.2 Pole orientation

We make several assumptions to constrain the pole orientation of 2I. The first is that the rotation period of 2I is shorter than the ~ 100 h. The longest known comet rotation period is for 1P/Halley of ~ 7.4 d ([Schleicher et al. 2015](#)), longer than the 2019 December 23-25 UTC observations, but the vast majority of known comet rotation periods are < 24 h ([Samarasinha et al. 2004](#); [Kokotanekova et al. 2017](#)). Additional evidence is that some comets have been observed to spin up as they enter the inner Solar System due to outgassing torques caused by the increasing sublimation of volatiles producing jets exerting recoil force on the comet decreasing their spin period below this 100 h limit (e.g., [Samarasinha et al. 1996](#); [Jewitt 1997](#); [Belton et al. 2011](#); [Samarasinha & Mueller 2013](#); [Bodewits et al. 2018](#)).

Our second assumption is that the comet is in a principal axis rotation state. One constraint on whether or not 2I is in a non-principal axis rotation state would be to observe the comet at the same viewing geometry spread out in time and observe if the jets' profile repeats themselves ([Samarasinha & Mueller 2002](#)). However, observations of 2I at repeating viewing geometries are not available given the comet's one-time trajectory through our Solar System.

Our third assumption is that the primary jet (i.e., the south-facing jet seen in the 2019 October-December and 2020 January images), is located on or in close proximity of the spin pole and is emitting dust in a cone centered on the rotation axis. Configurations where jets emanating from the spin pole axis is common in Solar System comets (eg., 17P/Borrelly [Farnham & Cochran 2002](#)). As seen in the observations taken on 2020 January 27 UTC during the Earth's crossing of the comet's orbital plane, the $\sim 30^\circ$ wide jet may lie within $\sim 10^\circ$ of the pole without affecting our pole orientation estimate. However, we caution this assumption with the fact that in the case of km-scale observations of the activity of 67P/Churyumov-Gerasimenko by *Rosetta* showed that the majority of dust was being ejected as a jet from the northern polar Hapi region ([Sierks et al. 2015](#); [Schmitt et al. 2017](#)), however, this polar jet feature was not seen in extensive imaging observations of 67P by *HST* and ground-based assets ([Snodgrass et al. 2017](#)).

Our fourth assumption is that the active region where the jet is located remains active throughout its entire rotation period. The jet could have a stationary appearance even if it is located near the equator of the comet if the activity ceases sporadically or periodically over the comet's rotation. In combination with the first two assumptions above, we expect that the comet's activity is always present through our observations.

With our assumptions about the location of the jet near the spin pole of 2I, its exact position projected into three dimensions can lie anywhere on a plane defined by the line-of-sight and jet position angle vectors for a given single observation ([Farnham & Cochran 2002](#)). By observing 2I at different viewing geometries, the pole/line-of-sight plane will shift where the intersection of these different planes will reveal which region in inertial space that the spin pole can be located compatible with all pole/line line-of-sight planes. We have thus computed the pole/line-of-sight planes given the measured jet position angle and viewing geometry for all 6 observing dates in Table 1 and have projected them into the celestial sphere as seen in Fig. 2. One curve is plotted per observing date listed in for a total of six curves that intersect within $\sim 10^\circ$ of

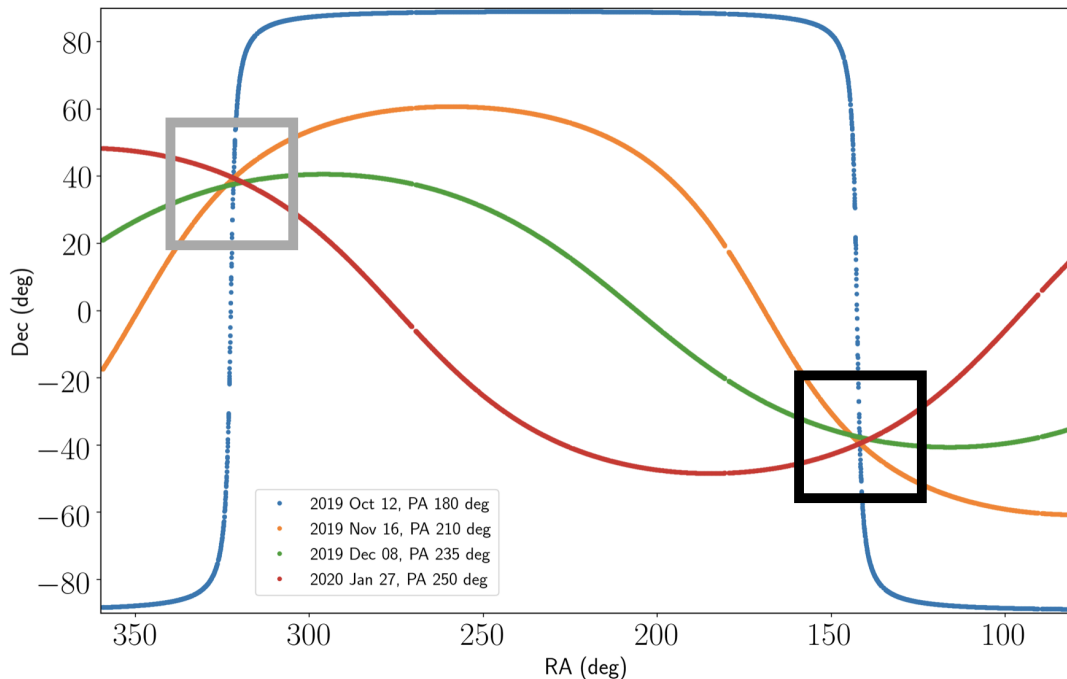


Figure 2. Pole/line-of-sight planes from the 4 observing dates in Table 1 projected on to the celestial sphere. The intersection zone of around $\alpha = 322^\circ$, $\delta = 37^\circ$ ($\lambda = 341^\circ$, $\beta = 48^\circ$) located in the grey square defines the rotation axis with an uncertainty of $\sim 10^\circ$. The intersection zone of around $\alpha = 141^\circ$, $\delta = -39^\circ$ ($\lambda = 162^\circ$, $\beta = -50^\circ$) located in the black square defines the antipodal solution with an uncertainty of $\sim 10^\circ$.

$\alpha = 322^\circ$, $\delta = 37^\circ$ ($\lambda = 341^\circ$, $\beta = 48^\circ$ in ecliptic coordinates) with an overall uncertainty of $\sim 10^\circ$. The close intersection of the pole/line-of-sight planes from observations at widely-spaced epochs suggest that the comet is in a mostly principle axis rotation state (Farnham & Cochran 2002). The uncertainty on the measured zone of convergence of the pole/line-of-sight planes is likely due to the $\sim 10^\circ$ uncertainty on our position angle measurements and the overall scatter around the convergence point. Non-principal axis rotation could cause a scatter in the observed pole/line-of-sight planes, but the effect may be small enough to produce an effect equivalent in magnitude to the uncertainty on the convergence zone caused by our position angle measurements. There is an ambiguity caused by the projection of the jet from the spin axis pole onto the celestial sphere that prevents us from knowing the sense of rotation.

The sub-Solar latitude as a function of time for our pole direction of 322° , $\delta = 37^\circ$ ($\lambda = 341^\circ$, $\beta = 48^\circ$) is presented in Fig. 3. Observed decreases in H_2O and dust production near perihelion (Xing et al. 2020; Cremonese et al. 2020; Bolin et al. 2020a) may be explained by seasonal effects that are evident around the time of perihelion where the pole is becomes increasingly face-on with the Solar direction starting from ~ 100 days before perihelion. This may have resulted in a decrease in temperature of relatively water-rich areas observed as a corresponding decrease in dust production and H_2O -driven activity. At the same time, spectroscopic observations of 2I from *HST* revealed that the CO production rate was increasing as the comet was nearing perihelion (Bodewits et al. 2020) which may suggest that the pole is rich in CO that was becoming more active as the pole was increasingly heated by the Sun.

Also presented in Fig. 3 is the sub-Solar latitude for the antipodal solution of $\alpha = 141^\circ$, $\delta = -39^\circ$ ($\lambda = 162^\circ$, $\beta = -50^\circ$). The antipodal solution isn't exactly 180° from the main pole solution due to the presence of scatter in the intersection of the Pole/line-of-sight planes in the antipodal direction as seen in Fig. 2. As the pole containing the primary jet becomes more face on with perihelion, its opposite pole becomes corresponding less face on entering polar night just after perihelion. As noted here and in *HST* images taken between 2019 October 12 UTC and 2019 December 6 UTC (see Fig. 6 Manzini et al. 2020) there is a second jet opposite the primary jet with a position angle $\sim 180^\circ$ in difference. Projection effects may be distorting the appearance of this second jet, but its $\sim 180^\circ$ difference in position angle from the primary jet may suggest it is located near the opposite hemisphere. As described by Manzini et al. (2020) and Kim et al. (2020), this second jet appears to decrease in intensity in *HST* images as the comet approaches perihelion completely disappearing in images taken on 2020 January 3 UTC. This may be explained by a decrease in activity on the pole opposite the primary jet as it enters polar night.

The pole solution of Manzini et al. (2020), $\alpha = 260^\circ$, $\delta = -35^\circ$ ($\lambda = 260^\circ$, $\beta = -11^\circ$) differs significantly from our result. To constrain the pole of 2I, Manzini et al. (2020) interpret the $\sim 180^\circ$ difference between the two jets seen in the 2019 October 12 UTC observations as the primary jet and secondary jets being located within located within $\sim 10^\circ$ of the comet's equator

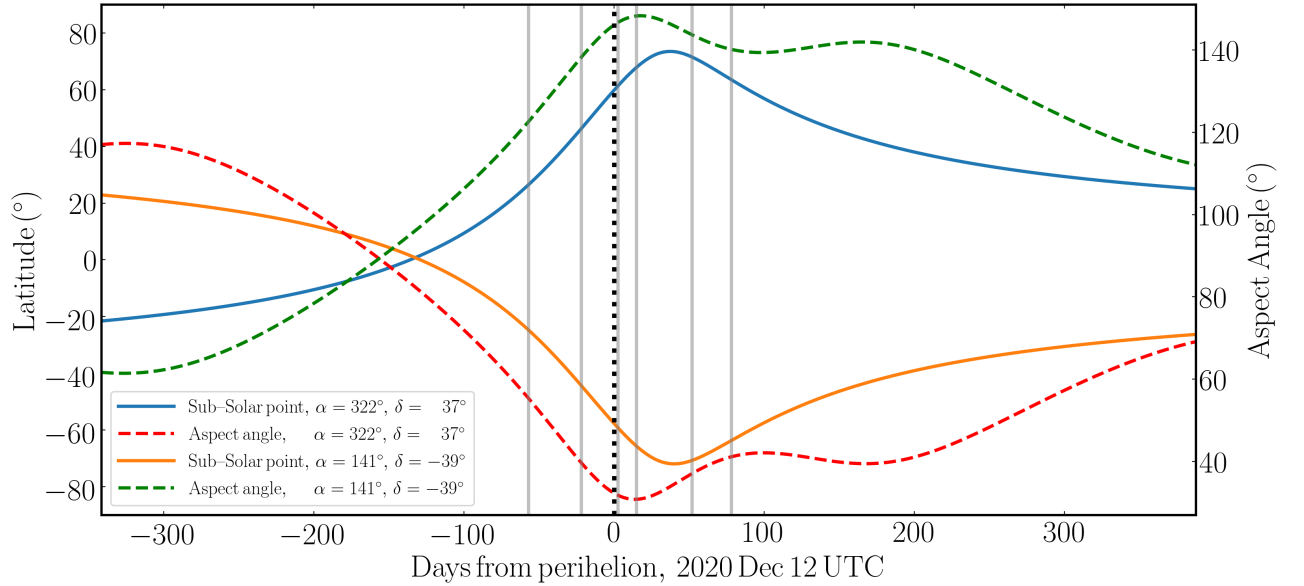


Figure 3. Time since perihelion (2019 December 8 UTC) vs. sub-Solar latitude angle for 2I with the pole solution of $\alpha = 322^\circ$, $\delta = 37^\circ$ ($\lambda = 341^\circ$, $\beta = 48^\circ$) as well as for the antipodal solution of $\alpha = 141^\circ$, $\delta = -39^\circ$ ($\lambda = 162^\circ$, $\beta = -50^\circ$) between 2019 January 01 and 2020 December 30. Also plotted is the aspect angle when viewed from the Earth, defined as is the angle between the pole and geocentric vectors centered on 2I. The time of the observations in Table 1 are plotted as vertical grey lines and the time of perihelion is plotted as a vertical black dotted line.

and that the spin axis is lying within the plane of the sky with a position angle of $\sim 100^\circ/280^\circ$. However, the near-equatorial position of the jets assumed by [Manzini et al. \(2020\)](#) are not compatible with our assumptions about the comet’s relatively short rotation period due to their stationary appearance in *HST* images discussed below in Section 4 and due to the polar appearance of jets of some comets. However, we do note that long-term observations of the activity of 67P by the *Rosetta* mission did not reveal jets occurring simultaneously from opposite poles ([Sierks et al. 2015](#)).

In addition, [Kim et al. \(2020\)](#) calculates a pole solution of $\alpha = 205^\circ$, $\delta = 52^\circ$ ($\lambda = 172^\circ$, $\beta = 56^\circ$) differing significantly from our result. They interpret the anisotropic morphology of the coma as consistent with the location of the peak mass loss located on the surface of the comet displaced from its local noon due to thermal lag (e.g., [Samarasinha et al. 2004](#)). Therefore the jet’s location in the thermal lag scenario is defined by its proximity towards the sub-Solar point and can therefore be located at a location off the spin pole axis unless pole is pointed in the direction of the Sun during its passage through the Solar System. According to Fig. 7 from ([Kim et al. 2020](#)), the sub-Solar point defined by their pole solution is located within $\sim 20^\circ$ of the comet’s equator during the comets travel through the Solar System covered by the *HST* which differs from our result. In addition, we note that the different assumptions in interpreting the pole solution in [Manzini et al. \(2020\)](#), [Kim et al. \(2020\)](#) and in this work lead to different pole solutions which may suggest current *HST* observations do not constrain a unique pole solution.

3.3 Photometry and lightcurves

We perform an independent analysis and calibration of the 2019 October 12 data presented in [Jewitt et al. \(2020a\)](#). We calculate the photometry on according to the aperture correction and zero-points determined for the F350LP filter ([Deustua et al. 2017](#)) and measure the photometry of 2I in the *HST* images using a circular aperture with an equivalent 10,000 km aperture resulting in $m_{F350LP} = 17.43 \pm 0.01$. Ground-based *V* filter observations of 2I by the MLO 1.0-m were conducted near simultaneously to the *HST* observations on 2019 October 12 UTC with the comet’s $V = 17.55 \pm 0.04$ ([Bolin et al. 2020a](#)) which we used to estimate the color between the F350LP and the *V* filters, $F350LP - V = -0.12 \pm 0.04$.

We then use the F350LP - *V* band color to determine the *V* magnitude in the 2019 October 12 observations using an aperture radius of $0.2''$ radius and a sky and outer coma subtraction annulus between $0.2-0.8''$ resulting in a *V* magnitude of 21.51 ± 0.04 . The smaller $0.2''$ radius aperture enabled by *HST* allows for the removal of orders of magnitude more light from the coma within the vicinity of the nucleus compared to ground-based observations enhancing the contrast between the coma nucleus (e.g. [Jewitt et al. 2019b](#)). We similarly use the $V-r = 0.45$, $V-i = 0.62$ and $V-z = 0.42$ colors of 2I/Borissov

taken from ground-based facilities (Bolin et al. 2020a) and absolute magnitude of the Sun from Willmer (2018) to calculate the equivalent V magnitude of 2I from the F689M and F845M data.

Using the following equation and the V magnitudes calculated above

$$H = V - 5 \log_{10}(r_h \Delta) - \Phi(\alpha) \quad (1)$$

we calculate the absolute magnitude H according to the heliocentric distance r_h in au and geocentric distance Δ in au from Table 1 and $\Phi(\alpha) = 0.04\alpha$, where α is the phase angle in degrees and 0.04 is the phase coefficient in magnitudes/degree, resulting in H magnitude of 16.59 ± 0.03 for the 2019 October 12 observations date. The rest of the H magnitude measurements for the data sets taken on other dates are listed in Table 1. We note that the errors on the H magnitudes may be underestimated in part due to the unknown phase function of 2I which might have a slightly larger phase coefficient than 0.04 magnitudes/degree.

As discussed in Jewitt (1991), the dilution of light from the nucleus by dust in the coma can dampen the variability in a comet lightcurve for timescales shorter than the crossing time of dust within the scale of the photometric aperture. For 2I, due to the density and slow crossing time of dust within its coma, measuring any short-term lightcurve variations on the order of hours to 10's of hours caused by the rotation of the comet's nucleus is difficult at the coarse resolution of ground-based observations (Jewitt & Luu 2019). We thus search instead for short-term variations in the lightcurve such as due to the rotation of the nucleus using the high-resolution WFC3/UVIS taken on 2019 October 12 UTC and in the data taken on 2019 December 23-25 UTC. At distances close to the surface of the comet, the speed of small, efficiently light scattering dust particles coupled directly to outflowing gas is approximately the speed of sound in gas (Jewitt 1991), 0.43 km/s at the black body temperature of the gas, 181 K, at the heliocentric distance of the comet of 2.37 au on 2019 October 12 UTC and 197 K at the heliocentric distance of the comet of 2.03 au on 2019 December 24 UTC. For ground-based observations taken with a 10,000 km aperture, this translates into a dust crossing time of $\gtrsim 10$ h. We can use the superb $0.04''/\text{pixel}$ (or ~ 60 km) resolution of the WFC3/UVIS data to measure the brightness of the comet with a smaller aperture enabling shorter coma dust dampening timescales.

For this analysis, we use a $0.2''$ radius aperture centered on the peak of the comet's brightness profile with a contiguous sky and outer coma subtraction aperture $0.2''-0.8''$. The equivalent distance spanning $0.2''$ at a distance of 2.79 au, the geocentric distance of 2I on 2019 October 12 UTC, is ~ 400 km and ~ 300 km at the geocentric distance of the comet of 1.93 au on 2019 December 24, 2019 UTC. These equivalent distances in 2019 October and November correspond to a crossing time of >10 h assuming a 1-10 m/s dust ejection velocity for mm-sized dust particles, which dominate the 2I dust cross-section as evidenced by ground and space-based observations (Cremonese et al. 2020; Hui et al. 2020; Kim et al. 2020). While the smaller $0.2''$ radius aperture enhances the contrast between the region containing the nucleus of the comet and the rest of the coma increasing the potential for measuring the variability of the lightcurve from the rotation of the comet's nucleus (e.g., Lamy et al. 1998a,b), the slow crossing time of the dust may prevent the measurement of periodic lightcurve variations shorter than ~ 10 h.

Our *HST* photometric measurements of 2I from *HST* observations taken on 2019 October 12 UTC are presented in Table 2 and in the top panel of Fig. 4. Our results are consistent with those of Jewitt et al. (2020a) showing only small variations in the lightcurve comparable to the $\gtrsim 0.01-0.02$ mag photometric uncertainties of individual datapoints which may be due to the slow crossing time of dust discussed above. The time of the observations has been corrected for light-travel time and the photometry has been kept in F350LP magnitude.

As an additional check, we have investigated the photometry of an additional set of observations of 2I were obtained with *HST* (HST GO 16043, PI Meech et al. 2019) that consisted of 14 orbits spread out over a ~ 70 h period between 2019 December 23 01:54:45 UTC and 2019 December 25 21:24:46 UTC. Observations during each of the 14 orbits on 2019 December 23-25 UTC resulted in 70 separate images with an equivalent exposure time of 380 s in the F350LP filter presented in. The lightcurve consisting of data points taken during 2019 December 23-25 UTC observations are presented in Table 3 and in the bottom panel of Fig. 4. There appears to be some variability on the scale of ~ 0.05 magnitude, at SNR 2.5 to 5.0.

Removing the linear trend fit over the data taken during the 2019 December 23-25 UTC and removing data points affected by background stars, we apply the Lomb-Scargle periodogram (Lomb 1976) to the data which is displayed in the top panel of Fig. 5. Removal of the linear trend over the three days observing period will affect the determination of rotation periods that are on multi-day time scales, but do not periodicities shorter than ~ 10 h time scales. The highest peak in the lightcurve period/rotation period vs. spectral power curve is located at ~ 5.3 h with a formal significance of $p \approx 10^{-6}$. We apply bootstrap estimation (Press et al. 1986) of the uncertainties by removing \sqrt{N} data points from the time series lightcurve and repeating our periodogram estimation of the rotation period 10,000 times resulting in a 1σ uncertainty estimate of ~ 0.1 h. As an independent check of our results obtained with the Lomb-Scargle periodogram, we apply phase dispersion minimization analysis to our data (Stellingwerf 1978) and obtain a result of ~ 10.6 h compatible with the rotation period estimate obtained with the Lomb-Scargle periodogram as seen in the second panel of Fig. 5.

We caution that although our periodogram analysis shows evidence for a periodic signal, it may be suspect because the single-peaked and double-peaked phased data as seen in the third panel indicate a small amplitude of only ~ 0.05 magnitudes (third and bottom panels, Fig. 5), comparable to within a factor of a few of the errors on the individual data points. Even

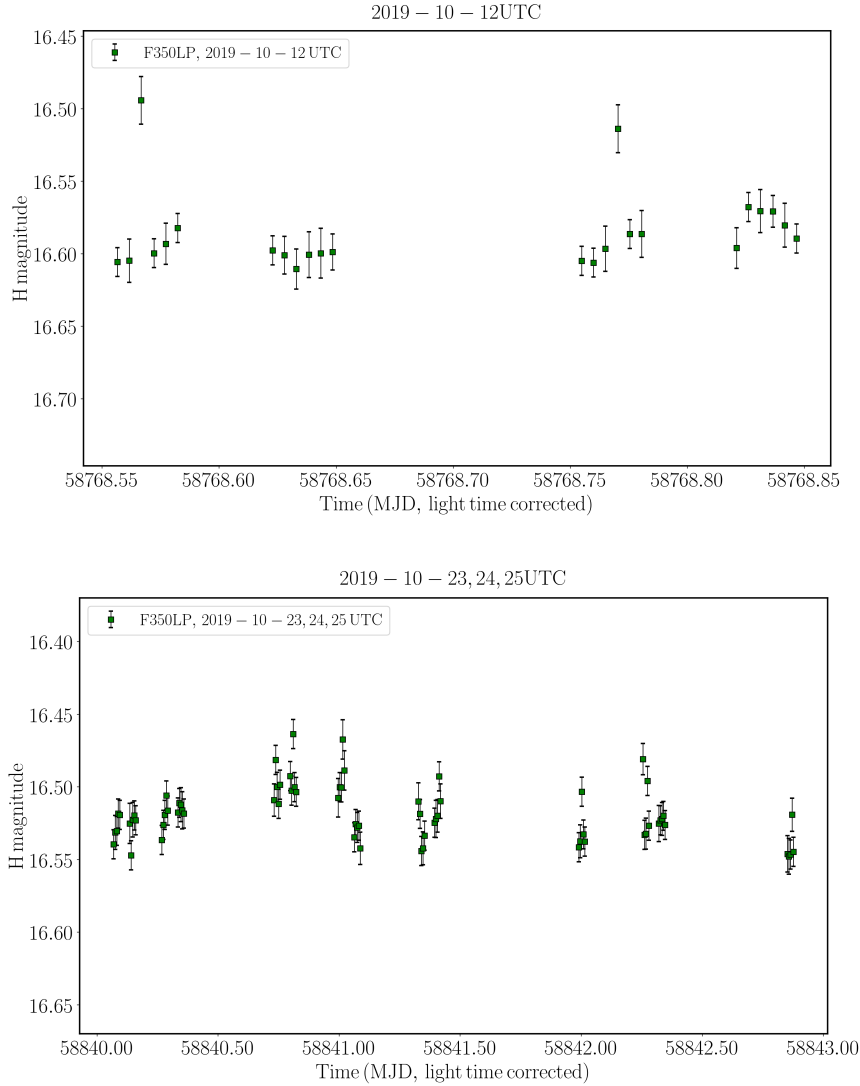


Figure 4. Top and bottom panels: WFC3/UVIS F350LP lightcurves of 2I taken on 2019 October 12 UTC and 2019 December 23-25 UTC. The photometry was measured using a $0.2''$ radius aperture radii. The overestimated data points in the first set of six and third set of six measurements are due to background stars coming into contact with the aperture centered on the brightest point of the comet. The error bars on the data points are equal to their 1σ photometric uncertainties. The data have been detrended and points affected by trailed background stars have been removed.

though small lightcurve amplitude might be expected in this case where the nucleus was not detected in the coma of this object (Bolin et al. 2020a; Jewitt et al. 2020a; Kim et al. 2020) due to the source within our photometric aperture being dominated by the coma’s dust (e.g., Hsieh et al. 2012), we note that the small lightcurve amplitude seen in observations of 2I is in stark contrast with the case of 1I/Oumuamua, which was observed to have >2 magnitude variations in its ~ 8 h rotation period lightcurve (Knight et al. 2017; Bolin et al. 2018). In addition, it has been shown in the case of 67P/Churyumov-Gerasimenko that significant variations of cometary activity can occur on hour timescales comparable crossing time of dust within the $0.2''$ radius aperture used to measure the photometry of the lightcurve (Lin et al. 2017).

4 DISCUSSION AND CONCLUSIONS

Although many observations of 2I have already occurred (e.g., Jewitt & Luu 2019; Fitzsimmons et al. 2019; Bolin et al. 2020a; Hui et al. 2020), our understanding of 2I and its context within the greater interstellar comet populations is only beginning to unfold. With the best-available spatial data of 2I, we have determined the existence of jet features in the coma surrounding the nucleus between 2019 October 12 UTC to 2020 January 27 UTC before and after its perihelion passage on 2019 December

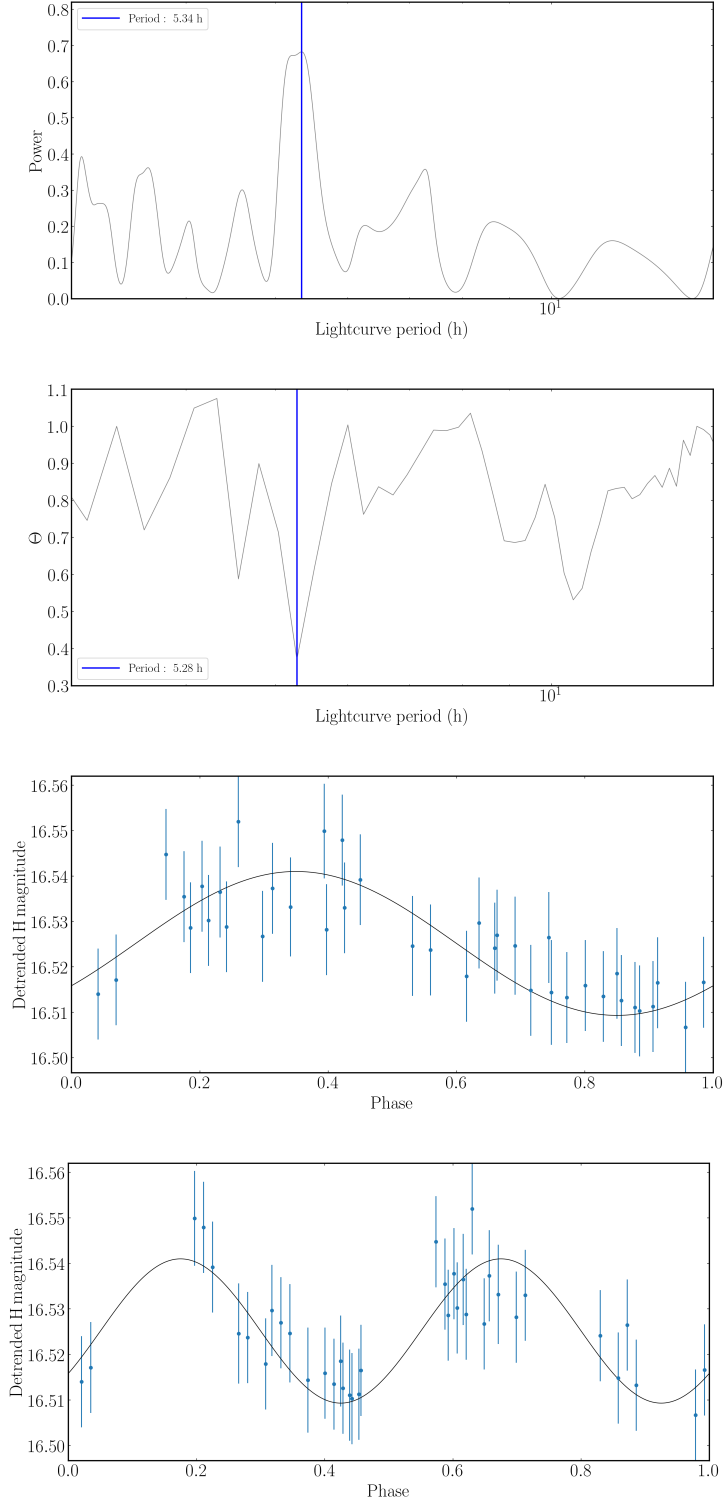


Figure 5. Top panel: Lomb-Scargle periodogram of lightcurve period vs spectral power (Lomb 1976) for the WFC3/UVIS F350LP lightcurve data from the 2019 December 23-25 UTC observations. A peak in the power is located at double-peaked rotation period of 10.67 h with a FWHM of ~ 0.1 h. Second panel: Phase dispersion minimization analysis of lightcurve rotation period vs. Θ metric (Stellingwerf 1978). The Θ metric is minimized at double-peaked rotation periods of 10.6 h consistent with the 10.67 h rotation period found with the Lomb-Scargle Periodogram. Third and fourth panel: phased WFC3/UVIS F350LP lightcurve using data from the 2019 December 23-25 UTC observations corresponding to a single-peak lightcurve period of 5.34 h and a double-peak lightcurve period of 10.68 h.

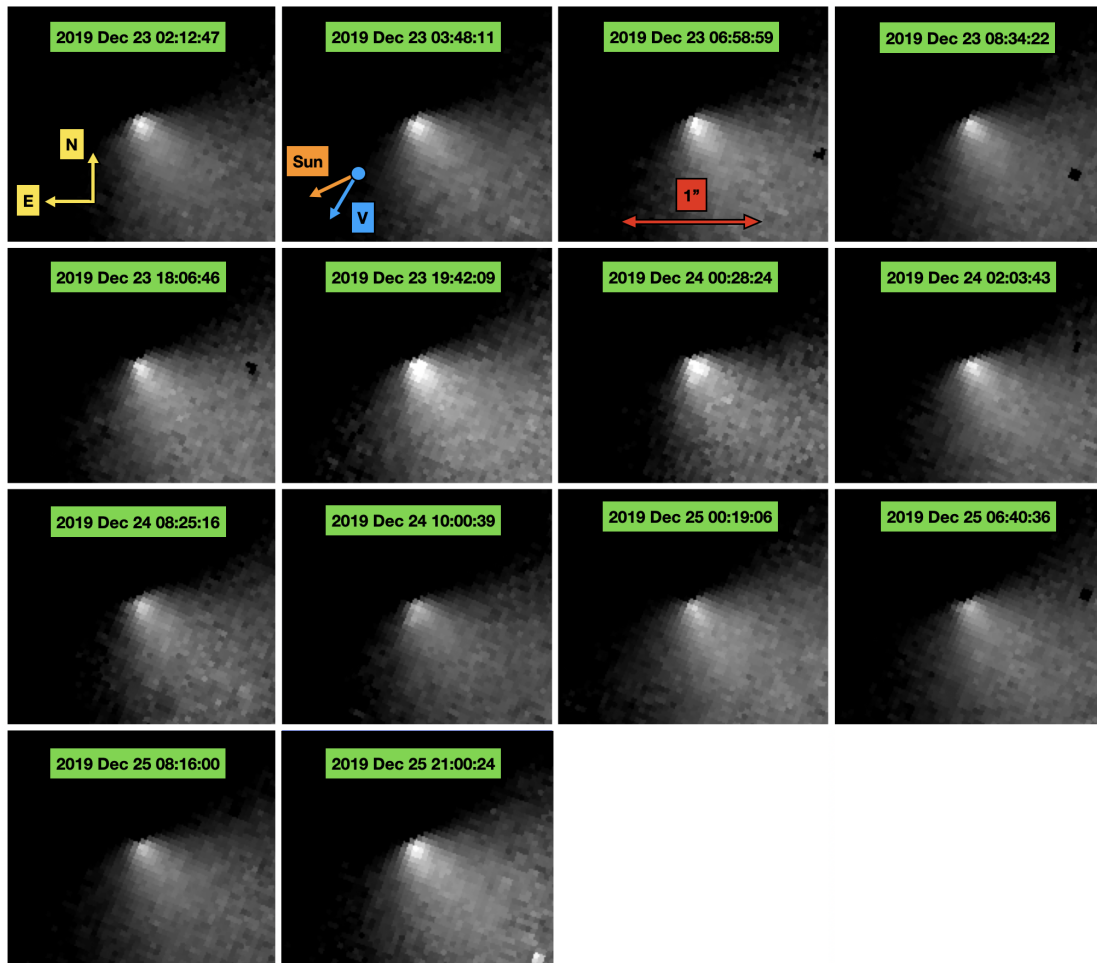


Figure 6. Mosaic of F350LP WFC3/UVIS images obtained over 14 orbits between 2019 December 23 02:12:47 UTC and 2019 December 25 21:00:24 UTC (HST GO 16043, Meech et al. 2019). Each panel is a median stack of five 380 s exposures obtained during each of the orbits resulting in an equivalent exposure time of 1900 s. The radial profile of the coma has been removed from the detection of 2I in each median stack. The cardinal direction vectors, the solar and orbital velocity and spatial scale are indicated.

8 UTC. Close time-series data taken on 2019 December 23-25 UTC show a possible ~ 0.05 magnitude lightcurve variations, however it is likely that these variations are not due to the rotation of the nucleus as a result of the comet’s cross-section being dominated by dust. Therefore, it may not be possible to constrain the rotation period of 2I with current *HST* observations.

We have used the ~ 5 month time span to determine the spin pole position of 2I finding that the data are consistent with the pole direction being towards $\alpha = 322^\circ$, $\delta = 37^\circ$ ($\lambda = 341^\circ$, $\beta = 48^\circ$) assuming that the jet is located near the comet’s rotation pole. Our assumptions are supported by checking the appearance of the jet in the 2019 December 23-25 UTC data seen in Fig. 6 which does not appear to significantly change its position angle over the ~ 70 h time span of the observations. The tight convergence of our pole/line-of-sight planes presented in Fig. 2 may imply that the comet is in a simple rotation state (Farnham & Cochran 2002) unlike 1I/‘Oumuamua which was observed to be in a tumbling rotational state (Fraser et al. 2018). However, given that three different assumptions lead to three different pole solutions as discussed in Section 3.2, we conclude that current *HST* observations of 2I may not provide a unique pole solution until additional observations are made that may provide additional evidence favoring particular assumptions.

If we assume that it is a rotating body whose shape is approximated by a triaxial prolate shape with dimensions with dimensions, $a:b:c$ where $b \geq a \geq c$ similar to Solar System comets (e.g., Binzel et al. 1989; Samarasinha et al. 2004), a small lightcurve amplitude of ~ 0.05 may imply a low b/a axial ratio of ~ 1 where $b/a = 10^{0.4A}$ where A is the peak-to-trough lightcurve amplitude (Binzel et al. 1989). The aspect angle between the observer’s line of sight and the rotational pole can affect the observed lightcurve amplitude where an object viewed pole on will appear to have a small lightcurve amplitude as the light-reflective cross-section when viewed at this angle is unchanging regardless of its shape (Barucci & Fulchignoni 1982). Although the light scattering cross-section of the nucleus is dust dominated in our observations even at the resolution enabled by *HST* and the lightcurve amplitude is very small at ~ 0.05 , we attempt to estimate a lower limit to the b/a taking

into account the aspect angle that 2I was viewed at during the 2019 December 23-25 UTC observations using the following

$$\Delta m_{\text{diff}} = 1.25 \log \left(\frac{b^2 \cos^2 \theta + c^2 \sin^2 \theta}{a^2 \cos^2 \theta + c^2 \sin^2 \theta} \right) \quad (2)$$

where a , b and c are the dimensions of 2I and θ is the aspect angle in degrees (Thirouin et al. 2016). We will assume $1 \lesssim b/a \lesssim 2$ typical for Solar System comets (Lamy et al. 2004) and that $a = c$ for a prolate triaxial ellipsoid. On 2019 December 23-25 UTC, 2I was observed at an aspect angle $\theta = 30^\circ$ as seen in Fig. 3 which combined with the above assumption results on 2I's triaxial shape results in a lightcurve amplitude correction of ~ 0.4 and $b/a = 10^{0.4A} \gtrsim 1.5$.

However, a nearly spherical body with a homogeneously reflective surface viewed equatorially would have a small lightcurve amplitude (Harris et al. 2014; Hanuš et al. 2018). In either of these cases, due to its dust-dominated coma observed in current *HST* data, it is not possible to tell if 2I has an extremely elongated shape like 1I/'Oumuamua (Bolin et al. 2018; Seligman & Laughlin 2020). Therefore, we present our results as demonstrating the non-uniqueness of inferred rotation properties of 2I using *HST* observations in its pre-Solar System encounter, pre-outburst rotational state (Jewitt et al. 2020b). Subsequent observations of 2I will be required to place more stringent constraints on its rotational state though may only be applicable to its post-outburst state and if the activity evolves so that the light scattering cross-section is less dust-dominated. Therefore, it may not be possible to fully constrain the rotation of 2I in its pre-Solar System encounter state.

ACKNOWLEDGEMENTS

Based on observations with the NASA/ESA Hubble Space Telescope obtained from the Data Archive at the Space Telescope Science Institute, which is operated by the Association of Universities for Research in Astronomy, Incorporated, under NASA contract NAS5-26555. Support for Program number (GO 16040) was provided through a grant from the STScI under NASA contract NAS5-26555.

We would like to acknowledge the anonymous reviewer whose helpful comments significantly improved the quality of this manuscript.

While this manuscript was in review, two other studies by Manzini et al. (2020) and Kim et al. (2020) focusing on the observations of 2I by *HST* and its pole solution were accepted and or submitted on arxiv respectively. The results in both papers complement our work and enhance the scientific discussion in this manuscript.

We would like to thank R. Jedicke and G. Helou for helpful discussion on the interpretation of low amplitude lightcurve data. We would also like to thank Y. R. Fernandez for helpful discussion on the interpretation of the comet coma data and for useful comments on constraining the pole. We thank D. Bodewits for advice in planning the *HST* observations and data reduction.

DATA AVAILABILITY

The data underlying this article will be shared on reasonable request to the corresponding author. The data are also available at the Mikulski Archive for Space Telescopes (MAST).

REFERENCES

- A'Hearn M. F., Millis R. C., Schleicher D. O., Osip D. J., Birch P. V., 1995, *Icarus*, **118**, 223
 Bannister M. T., et al., 2020, arXiv e-prints, p. [arXiv:2001.11605](https://arxiv.org/abs/2001.11605)
 Barucci M. A., Fulchignoni M., 1982, *Moon and Planets*, **27**, 47
 Belton M. J. S., et al., 2011, *Icarus*, **213**, 345
 Binzel R. P., Farinella P., Zappalà V., Cellino A., 1989, in Binzel R. P., Gehrels T., Matthews M. S., eds, *Asteroids II*. pp 416–441
 Bodewits D., Farnham T. L., Kelley M. S. P., Knight M. M., 2018, *Nature*, **553**, 186
 Bodewits D., et al., 2020, *Nature Astronomy*,
 Bolin B. T., et al., 2018, *ApJ*, **852**, L2
 Bolin B. T., Bodewits D., Fernandez Y., Lisse C. M., 2019, Constraining the coma volatile content of interstellar comet 2I/Borisov, *HST Proposal*
 Bolin B. T., et al., 2020a, *AJ*, **160**, 26
 Bolin B. T., Bodewits D., Lisse C. M., Fernandez Y. R., Helou G., Cenko S. B., 2020b, *The Astronomer's Telegram*, **13613**, 1
 Cordiner M. A., et al., 2020, *Nature Astronomy*,
 Cremonese G., et al., 2020, *ApJ*, **893**, L12
 Crovisier J., Colom P., Biver N., Bockelee-Morvan D., 2019, *Central Bureau Electronic Telegrams*, **4691**
 Deustua S. E., Mack J., Bajaj V., Khandrika H., 2017, Technical report, WFC3/UVIS Updated 2017 Chip-Dependent Inverse Sensitivity Values
 Drahus M., et al., 2020, *The Astronomer's Telegram*, **13549**, 1
 Dressel L., 2012, *Wide Field Camera 3 Instrument Handbook for Cycle 21 v. 5.0*

- Farnham T. L., 2009, *Planet. Space Sci.*, **57**, 1192
- Farnham T. L., Cochran A. L., 2002, *Icarus*, **160**, 398
- Fitzsimmons A., et al., 2019, *ApJ*, **885**, L9
- Fraser W. C., Pravec P., Fitzsimmons A., Lacerda P., Bannister M. T., Snodgrass C., Smolić I., 2018, *Nature Astronomy*, **2**, 383
- Guzik P., Drahus M., Rusek K., Waniak W., Cannizzaro G., Pastor-Marazuela I., 2019, *Nature Astronomy*, p. 467
- Hanuš J., et al., 2018, *Icarus*, **299**, 84
- Harris A. W., et al., 2014, *Icarus*, **235**, 55
- Hsieh H. H., Yang B., Haghighipour N., 2012, *ApJ*, **744**, 9
- Hui M.-T., Ye Q.-Z., Föhning D., Hung D., Tholen D. J., 2020, arXiv e-prints, p. [arXiv:2003.14064](https://arxiv.org/abs/2003.14064)
- Jehin E., Moulane F., Pozuelos M., Manfroid J., 2020, Central Bureau Electronic Telegrams, 4729
- Jewitt D., 1991, in Newburn Jr. R. L., Neugebauer M., Rahe J., eds, *Astrophysics and Space Science Library* Vol. 167, IAU Colloq. 116: Comets in the post-Halley era. pp 19–65, doi:10.1007/978-94-011-3378-4_2
- Jewitt D., 1997, *Earth Moon and Planets*, **79**, 35
- Jewitt D., Luu J., 2019, *ApJ*, **886**, L29
- Jewitt D., Mutchler M., Kim Y., Weaver H., 2019a, Interstellar Object C/2019 Q4, HST Proposal
- Jewitt D., Agarwal J., Hui M.-T., Li J., Mutchler M., Weaver H., 2019b, *AJ*, **157**, 65
- Jewitt D., Hui M.-T., Kim Y., Mutchler M., Weaver H., Agarwal J., 2020a, *ApJ*, **888**, L23
- Jewitt D., Kim Y., Mutchler M., Weaver H., Agarwal J., Hui M.-T., 2020b, *ApJ*, **896**, L39
- Kareta T., et al., 2019, arXiv e-prints, p. [arXiv:1910.03222](https://arxiv.org/abs/1910.03222)
- Kim Y., Jewitt D., Mutchler M., Agarwal J., Hui M.-T., Weaver H., 2020, arXiv e-prints, p. [arXiv:2005.02468](https://arxiv.org/abs/2005.02468)
- Knight M. M., Schleicher D. G., 2013, *Icarus*, **222**, 691
- Knight M. M., Protopapa S., Kelley M. S. P., Farnham T. L., Bauer J. M., Bodewits D., Feaga L. M., Sunshine J. M., 2017, preprint, ([arXiv:1711.01402](https://arxiv.org/abs/1711.01402))
- Kokotanekova R., et al., 2017, *MNRAS*, **471**, 2974
- Lamy P. L., Toth I., Jorda L., Weaver H. A., A'Hearn M., 1998a, *A&A*, **335**, L25
- Lamy P. L., Toth I., Weaver H. A., 1998b, *A&A*, **337**, 945
- Lamy P. L., Toth I., Fernandez Y. R., Weaver H. A., 2004, The sizes, shapes, albedos, and colors of cometary nuclei. p. 223
- Lin Z.-Y., et al., 2017, *MNRAS*, **469**, S731
- Lomb N. R., 1976, *Ap&SS*, **39**, 447
- Manzini F., Oldani V., Ochner P., Bedin L. R., . 2020, arXiv e-prints, p. [arXiv:2004.02033](https://arxiv.org/abs/2004.02033)
- McKay A. J., Cochran A. L., Dello Russo N., DiSanti M., 2019, arXiv e-prints, p. [arXiv:1910.12785](https://arxiv.org/abs/1910.12785)
- Meech K., Buie M., Keane J., Kleyna J., Hainaut O., 2019, Characterization of the second interstellar object, HST Proposal
- Opitom C., et al., 2019, arXiv e-prints, p. [arXiv:1910.09078](https://arxiv.org/abs/1910.09078)
- Press W. H., Flannery B. P., Teukolsky S. A., 1986, *Numerical recipes. The art of scientific computing*
- Samarasinha N. H., Mueller B. E. A., 2002, *Earth Moon and Planets*, **90**, 473
- Samarasinha N. H., Mueller B. E. A., 2013, *ApJ*, **775**, L10
- Samarasinha N. H., Mueller B. E. A., Belton M. J. S., 1996, *Planet. Space Sci.*, **44**, 275
- Samarasinha N. H., Mueller B. E. A., Belton M. J. S., Jorda L., 2004, Rotation of cometary nuclei. pp 281–299
- Schleicher D. G., Farnham T. L., 2004, Photometry and imaging of the coma with narrowband filters. p. 449
- Schleicher D. G., Bair A. N., Sackey S., Alciatore Stinnett L. A., Williams R. M. E., Smith-Konter B. R., 2015, *AJ*, **150**, 79
- Schmitt M. I., et al., 2017, *MNRAS*, **469**, S380
- Seligman D., Laughlin G., 2020, arXiv e-prints, p. [arXiv:2005.12932](https://arxiv.org/abs/2005.12932)
- Sierks H., et al., 2015, *Science*, **347**, aaa1044
- Snodgrass C., et al., 2017, *Philosophical Transactions of the Royal Society of London Series A*, **375**, 20160249
- Stellingwerf R. F., 1978, *ApJ*, **224**, 953
- Thirouin A., et al., 2016, *AJ*, **152**, 163
- Willmer C. N. A., 2018, *ApJS*, **236**, 47
- Xing Z., Bodewits D., Noonan J., Bannister M. T., 2020, arXiv e-prints, p. [arXiv:2001.04865](https://arxiv.org/abs/2001.04865)
- Yang B., Kelley M. S. P., Meech K. J., Keane J. V., Protopapa S., Bus S. J., 2020, *A&A*, **634**, L6
- Ye Q., et al., 2019, arXiv e-prints, p. [arXiv:1911.05902](https://arxiv.org/abs/1911.05902)
- de León J., Licandro J., Serra-Ricart M., Cabrera-Lavers A., Font Serra J., Scarpa R., de la Fuente Marcos C., de la Fuente Marcos R., 2019, *Research Notes of the American Astronomical Society*, **3**, 131

Table 2: Summary of comet 2I photometry taken on 2019 October 12 UTC.

Date ¹ UTC	Filter ²	Exp ³ (s)	H^4
58768.5565711	F350LP	260 s	16.61 ± 0.02
58768.5616289	F350LP	260 s	16.60 ± 0.01
58768.5666868	F350LP	260 s	16.49 ± 0.02
58768.5721266	F350LP	260 s	16.60 ± 0.02
58768.5771845	F350LP	260 s	16.59 ± 0.01
58768.5822424	F350LP	260 s	16.58 ± 0.01
58768.6227863	F350LP	260 s	16.60 ± 0.01

Continued on next page

Table 2 – Continued from previous page

Date ¹ UTC	Filter ²	Exp ³ (s)	H ⁴
58768.6278442	F350LP	260 s	16.60 ± 0.01
58768.6329021	F350LP	260 s	16.61 ± 0.01
58768.6383419	F350LP	260 s	16.60 ± 0.01
58768.6433998	F350LP	260 s	16.60 ± 0.01
58768.6484576	F350LP	260 s	16.60 ± 0.01
58768.7547887	F350LP	260 s	16.60 ± 0.02
58768.7598465	F350LP	260 s	16.61 ± 0.01
58768.7649044	F350LP	260 s	16.60 ± 0.02
58768.7703442	F350LP	260 s	16.51 ± 0.02
58768.7754021	F350LP	260 s	16.59 ± 0.02
58768.78046	F350LP	260 s	16.59 ± 0.01
58768.8209924	F350LP	260 s	16.60 ± 0.01
58768.8260502	F350LP	260 s	16.57 ± 0.01
58768.8311081	F350LP	260 s	16.57 ± 0.01
58768.8365479	F350LP	260 s	16.57 ± 0.02
58768.8416058	F350LP	260 s	16.58 ± 0.01
58768.8466637	F350LP	260 s	16.59 ± 0.01

Table 2: Columns: (1) observation date correct for light travel time; (2) *HST*/WFC3 Filter; (3) Exposure time (4) H magnitude with 1 σ uncertainties

Table 3: Summary of comet 2I photometry taken on 2019 December 23-25 UTC.

Date ¹ UTC	Filter ²	Exp ³ (s)	H ⁴
58840.0684946	F350LP	380 s	16.54 ± 0.01
58840.0747562	F350LP	380 s	16.53 ± 0.01
58840.0810178	F350LP	380 s	16.53 ± 0.01
58840.0872794	F350LP	380 s	16.52 ± 0.01
58840.0935409	F350LP	380 s	16.52 ± 0.01
58840.1347446	F350LP	380 s	16.53 ± 0.01
58840.1410062	F350LP	380 s	16.55 ± 0.01
58840.1472678	F350LP	380 s	16.52 ± 0.01
58840.1535294	F350LP	380 s	16.52 ± 0.01
58840.1597909	F350LP	380 s	16.52 ± 0.01
58840.2672446	F350LP	380 s	16.54 ± 0.01
58840.2735062	F350LP	380 s	16.53 ± 0.01
58840.2797678	F350LP	380 s	16.52 ± 0.01
58840.2860294	F350LP	380 s	16.51 ± 0.01
58840.2922909	F350LP	380 s	16.52 ± 0.01
58840.3334831	F350LP	380 s	16.52 ± 0.01
58840.3397446	F350LP	380 s	16.51 ± 0.01
58840.3460062	F350LP	380 s	16.51 ± 0.01
58840.3522678	F350LP	380 s	16.52 ± 0.01
58840.3585294	F350LP	380 s	16.52 ± 0.01
58840.7309831	F350LP	380 s	16.51 ± 0.01
58840.7372446	F350LP	380 s	16.48 ± 0.01
58840.7435062	F350LP	380 s	16.5 ± 0.01
58840.7497678	F350LP	380 s	16.51 ± 0.01
58840.7560294	F350LP	380 s	16.5 ± 0.01
58840.7972215	F350LP	380 s	16.49 ± 0.01

Continued on next page

Table 3 – *Continued from previous page*

Date ¹ UTC	Filter ²	Exp ³ (s)	H^4
58840.8034831	F350LP	380 s	16.5 ± 0.01
58840.8097446	F350LP	380 s	16.46 ± 0.01
58840.8160062	F350LP	380 s	16.5 ± 0.01
58840.8222678	F350LP	380 s	16.5 ± 0.01
58840.9960062	F350LP	380 s	16.51 ± 0.01
58841.0022678	F350LP	380 s	16.5 ± 0.01
58841.0085294	F350LP	380 s	16.5 ± 0.01
58841.0147909	F350LP	380 s	16.47 ± 0.01
58841.0210525	F350LP	380 s	16.49 ± 0.01
58841.0621983	F350LP	380 s	16.53 ± 0.01
58841.0684599	F350LP	380 s	16.53 ± 0.01
58841.0747215	F350LP	380 s	16.53 ± 0.01
58841.0809831	F350LP	380 s	16.53 ± 0.01
58841.0872446	F350LP	380 s	16.54 ± 0.01
58841.3271636	F350LP	380 s	16.51 ± 0.01
58841.3334252	F350LP	380 s	16.52 ± 0.01
58841.3396868	F350LP	380 s	16.54 ± 0.01
58841.3459483	F350LP	380 s	16.54 ± 0.01
58841.3522099	F350LP	380 s	16.53 ± 0.01
58841.393402	F350LP	380 s	16.52 ± 0.01
58841.3996636	F350LP	380 s	16.52 ± 0.01
58841.4059252	F350LP	380 s	16.52 ± 0.01
58841.4121868	F350LP	380 s	16.49 ± 0.01
58841.4184483	F350LP	380 s	16.51 ± 0.01
58841.9895479	F350LP	380 s	16.54 ± 0.01
58841.9958095	F350LP	380 s	16.54 ± 0.01
58842.002071	F350LP	380 s	16.5 ± 0.01
58842.0083326	F350LP	380 s	16.53 ± 0.01
58842.0145942	F350LP	380 s	16.54 ± 0.01
58842.2544784	F350LP	380 s	16.48 ± 0.01
58842.26074	F350LP	380 s	16.53 ± 0.01
58842.2670016	F350LP	380 s	16.53 ± 0.01
58842.2732632	F350LP	380 s	16.5 ± 0.01
58842.2795247	F350LP	380 s	16.53 ± 0.01
58842.3207284	F350LP	380 s	16.53 ± 0.01
58842.32699	F350LP	380 s	16.52 ± 0.01
58842.3332516	F350LP	380 s	16.52 ± 0.01
58842.3395132	F350LP	380 s	16.52 ± 0.01
58842.3457747	F350LP	380 s	16.53 ± 0.01
58842.8515618	F350LP	380 s	16.55 ± 0.01
58842.8578233	F350LP	380 s	16.55 ± 0.01
58842.8640849	F350LP	380 s	16.55 ± 0.01
58842.8703465	F350LP	380 s	16.52 ± 0.01
58842.8766081	F350LP	380 s	16.54 ± 0.01

Table 3: Columns: (1) observation date correct for light travel time; (2) *HST*/WFC3 Filter; (3) Exposure time (4) H magnitude with 1 σ uncertainties